Enhanced broadband optical limiting and switching of nonlinear absorption in functionalized solar exfoliated reduced graphene oxide–Ag-Fe_2O_3 nanocomposites

T. C. Sabari Girisun, M. Saravanan, and S. Venugopal Rao

Citation: Journal of Applied Physics **124**, 193101 (2018); doi: 10.1063/1.5050478
View online: https://doi.org/10.1063/1.5050478
View Table of Contents: http://aip.scitation.org/toc/jap/124/19
Published by the American Institute of Physics

JOURNAL OF APPLIED PHYSICS **124**, 193101 (2018)

Enhanced broadband optical limiting and switching of nonlinear absorption in functionalized solar exfoliated reduced graphene oxide–Ag-Fe_2O_3 nanocomposites

T. C. Sabari Girisun,[1,a)] M. Saravanan,[1] and S. Venugopal Rao[2,b)]
[1]*Nanophotonics Laboratory, Department of Physics, Bharathidasan University, Tiruchirappalli 620024, Tamilnadu, India*
[2]*Advanced Centre of Research in High Energy Materials (ACRHEM), University of Hyderabad, Hyderabad 500046, Telangana, India*

(Received 31 July 2018; accepted 27 October 2018; published online 15 November 2018)

Wavelength dependent nonlinear absorption (NLA) studies of Ag-Fe_2O_3–reduced graphene oxide (rGO) hybrids were performed using high-repetition rate (80 MHz), femtosecond (150 fs), and near-infrared (NIR) (700-900 nm) laser pulses. Tunable nonlinear absorption properties and broadband optical limiting performance of the pure and Ag-Fe_2O_3–(15, 25, and 40 wt. %) rGO nanocomposites were achieved by varying the parameters such as composition, defect states, and morphology. Detailed Z-scan experiments revealed that the NLA coefficient increases with an increase in the excitation wavelength. A switching behavior in the NLA mechanism for Ag-Fe_2O_3 and Ag-Fe_2O_3–(15 wt. %)rGO from saturable absorption (700 nm) to reverse saturable absorption (800 nm and 900 nm) was witnessed, while rGO and Ag-Fe_2O_3–(25 wt. % and 40 wt. %)rGO exhibited reverse saturable absorption, which is ascribed to be the 2-photon absorption (2PA) process. The origin of 2PA involves the electronic states of irregular conjugate carbon bonds based on sp^2 domains of rGO for 700 nm and 800 nm excitations and surface plasmon resonance of Ag metals for 900 nm excitations. Ag-Fe_2O_3–(25 wt. %)rGO hybrid possesses a stronger NLA coefficient and a lower onset optical limiting threshold at all the wavelengths studied and, therefore, can be considered as a favorable candidate for broadband ultrafast optical limiters toward protection from NIR ultrashort pulse laser damages. *Published by AIP Publishing.* https://doi.org/10.1063/1.5050478

I. INTRODUCTION

In the modern era of lasers and photonics, ultrashort lasers [pulse width of a few tens of femtoseconds (fs)] find enormous applications and are rapidly replacing the conventional lasers. These ultrafast lasers deliver a tremendously high pulse peak intensity with ultrashort temporal resolution, thus making them indispensable in the fields of optical communication, femto-chemistry, high precision material processing, micro-fabrication, bio-imaging, photodynamic therapy, and laser microsurgery.[1–7] Particularly, longer wavelength near-infrared (NIR) femtosecond lasers are exhaustively explored in the development of the infrared (1400-1600 nm) pulsed laser in the telecommunication wavelengths with frequency tunability, as they are capable of generating shorter wavelengths through second-order nonlinear optical (NLO) processes such as second harmonic generation.[8] Hence, beyond technological advancements, prime importance is given to the domain of ultrafast nonlinear optical (NLO) studies that originates from the interaction of high intense ultrashort pulse laser with matter. Intensity dependent nonlinear absorption (NLA) is one of the most important scientific phenomena, which has the capacity to open up plenty of new applications. This energy absorbing nonlinear process can be broadly classified as saturable absorption (SA) (increased transmittance) and reverse saturable absorption (RSA) (decreased transmittance).[9] Saturable absorption (SA) is broadly utilized in nonlinear optical modulators which are used in mode-locking and passive Q-switching techniques for the generation of ultrashort pulse lasers, and reverse saturable absorbers can be used as optical limiters toward the protection of sensitive optical components including human eyes from laser induced damages.[10–12] These phenomena are strongly intensity dependent (in general, SA is seen at lower laser fluence and RSA becomes predominant at higher laser fluence) and can be specifically induced in a material by a proper choice of the excitation source. Therefore, it is always an interesting subject of research to understand the wavelength dependent nonlinear absorption of the material, as it offers the tool to modulate light intensity. In particular, broadband optical limiting (BOL) materials that can be used as laser safety devices against the range of wavelengths are in the limelight.

Materials displaying multi-photon absorption (MPA) properties could address various optical limiting (OL) applications such as protection of LIDAR detectors and imagery systems and erbium amplifier gain equalization.[13,14] An efficient optical limiter demands a number of requirements such as high transmission for weak signals, ultrafast response, sufficiently wide broadband, and negligible beam quality degradations. In particular, ultrafast optical nonlinearity based broadband optical limiters are desirable and yet to be developed. Most of the optical limiters reported are confined to nanosecond pulse laser excitation, and femtosecond pulse

[a)]Author to whom correspondence should be addressed: sabarigirisun@bdu.ac.in. Tel.: +91 9865783510.
[b)]E-mail: soma_venu@uohyd.ac.in

laser excited optical limiters are comparatively less common. Our current interest in graphene nanosheets (a single layer of graphene absorbs 2.3% of the incident white light)[15] involves their chemical functionalization to yield new materials with broadband optical limiting behavior against NIR ultrafast pulse lasers. The carbon 2D sheet with sp^2 carbon offers a strong aromatic interaction with analytes through hydrophobic and π-π stacking.[16] Hence, it appears as a suitable platform for molecular tailoring, thereby fulfilling the prerequisite for broadband optical limiting applications. Accordingly, in 2D layered materials, graphene along with its oxide derivatives such as graphene oxide (GO) and reduced graphene oxides (rGO) has recently been explored as potential materials for various laser applications.[17–20] The presence of the functional groups transforms some of the sp^2 carbons to sp^3 ones, resulting in structural defects that give GO and rGO a finite bandgap and forming many isolated sp^2 carbon sites. These carbonaceous materials with higher carrier mobility provide rapid cooling after laser excitation, and the smaller density of state (DOS) near the Femi level presents a bottleneck for mid-IR range nonlinear absorption.[21,22]

The band structure of free graphene can be modified through two-way charge transfer as metal nanoparticles (NPs) are brought to close proximity of the surface of graphene. Graphene with wrinkled sheets when compared with pristine graphene has advantages of accommodating metal nanoparticles, which in turn provide the broadband absorption regions. In the choice of metal nanoparticles, silver has received much attention due to its intriguing properties such as strong visible region surface plasmon resonance (SPR).[15,23] The plasmon resonance of these metal nanoparticles can cause enhancement of the local electric field and thus leads to many interesting optical properties. Furthermore, it is to be noted that heterostructures or composites that contain magnetic particles and NLO material offer interaction between magnetic susceptibility and nonlinear absorption, which can be utilized to realize magneto-controlled NLO materials. Magnetic fluids that contain Fe_2O_3 particles especially offer tunable linear and nonlinear absorption through varying magnetic field as a consequence of anisotropy induced by the orientation of suspended particles. A recent report on Ag-Fe_2O_3 composite revealed the band structure tunability and improved the NLO performance with fs (780 nm, 1 kHz) laser excitation.[24] Z-scan experiments on silver-decorated graphene (Ag NP/fG) depicted that the effect of SA becomes stronger at 1064 nm with silver decoration, and with increasing the intensity, the effect of reverse saturable absorption (RSA) is observed, indicating promising optical limiting (OL).[25] Also, both nonlinear absorption and nonlinear refraction of Ag NPs/rGO can be effectively enhanced by the hybridization of Ag NPs.[26] Hence, the combination of Ag, Fe_2O_3, and rGO can offer tunable band structure which can be utilized for the realization of BOL action and for enhancing the third-order NLO properties. The context of this article is to report the optical nonlinearity of solution-processed plasmonic (Ag) semiconductor (Fe_2O_3)–reduced graphene oxide nanocomposite under ultrafast pulse laser excitations, which is characterized for broadband and tunable spectral response.

II. RESULTS AND DISCUSSION

A. Wavelength dependent nonlinear absorption

Wavelength dependent nonlinear absorption of rGO, Ag-Fe_2O_3, and Ag-Fe_2O_3-(15, 25, and 40 wt. %)rGO was evaluated by open-aperture Z-scan measurements with excitation source as a mode-locked Ti:Sapphire oscillator-seeded regenerative amplifier that gives output laser pulses from a tunable oscillator (Chameleon, coherent) having wavelengths of 700-900 nm with a pulse duration of 150 fs at a repetition rate of 80 MHz. The input beam was focused using a plano convex lens (focal length, $f = 100$ mm) on the sample whose input energy was attenuated using a set of neutral density filters. As the beam waist ($\omega_0 = 2f\lambda/\pi D$) of the pulse is directly proportional to the wavelength of excitation (λ), it varies as 22.3 μm (700 nm), 25.5 μm (800 nm), and 28.7 μm (900 nm). Along the direction of the focused beam, the sample taken in a cuvette was moved using a translation system, and its corresponding far-field output transmittance was measured. The path length of the sample (1 mm) was less than the Rayleigh range [$Z_0 = 2.2$ mm (700 nm), 2.54 mm (800 nm), and 2.86 mm (900 nm)] for all chosen wavelengths and thus satisfies the Z-scan condition for the thin sample limit. For different wavelengths, a typical input power of 3 mW was used and the corresponding peak intensities, $I_0 = 2\ P/\pi\omega_0^2 = 4\sqrt{\ln 2}\varepsilon/\pi^{3/2}\omega_0^2 t_{FWHM} = 2E/\pi\omega_0^2 t_{FWHM}$, with P as the average peak power, E and t_{FWHM} as the energy and pulse width,[27,28] were estimated to be 320 MW/cm^2 (700 nm), 245 MW/cm^2 (800 nm), and 193 MW/cm^2 (900 nm). This change in the peak intensity with respect to the wavelength of the laser source is a critical element, as the observed nonlinear absorption is intensity dependent governed by the relation $\alpha(I) = \alpha/1 + I/I_s + \beta_{eff}I$. Hence, with a change in the wavelength of excitation, the observed nonlinear absorption coefficient varies significantly.

The wavelength dependent NLO properties of the synthesized nanocomposites were studied using the Z-scan technique. The nanocomposites were dispersed in ethylene glycol through ultrasonication, and the studies were performed on the nanocomposites with a concentration of 5 mg/5 ml. By adding ethylene glycol to the Ag-Fe_2O_3–rGO nanocomposite solutions, the linear transmittance of the solution was adjusted to be ~70% (in the 700-900 nm range). In the open aperture (OA) mode, the transmitted beam was totally collected using a lens placed in front of the photo-detector. The Z-scan data are strongly dependent on the experimental conditions such as nature of the samples and pulse characteristics. It is pertinent to note that the presence of even a small linear absorption can result in a large nonlinear absorption, depending on the repetition rate of the laser and on the thermo-optical properties of the sample material.[29,30] The OA Z-scan data provide information about the NLA that can occur via genuine/instantaneous multi-photon absorption (MPA) involving simultaneous absorption of two or more photons or excited state absorption (ESA) involving sequential absorption of two or more photons.[31,32] By fitting the experimental results, it is possible to obtain the magnitude of NLA. Nonlinear transmission described by the basic MPA with two photon absorption called as the 2PA type process

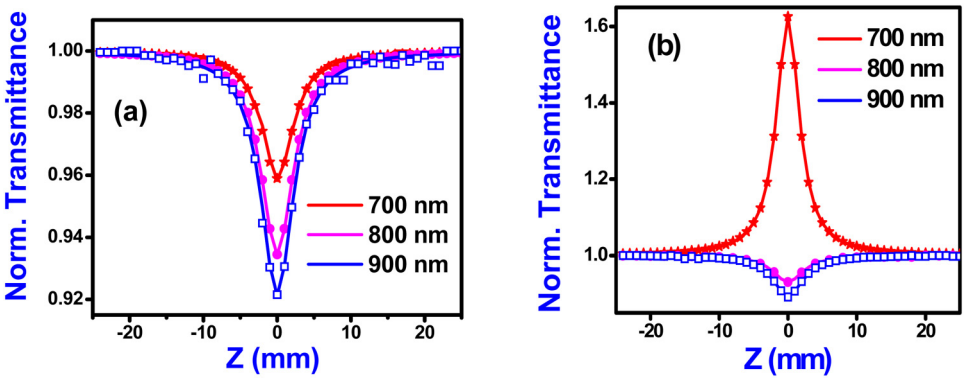

FIG. 1. Open aperture Z-scan patterns of pure (a) rGO and (b) Ag-Fe_2O_3 excited with different NIR wavelengths.

can be obtained by solving the pulse propagation equation[27]

$$\frac{dI}{dz'} = -\frac{\alpha_0 I}{1 + I/I_s} - \beta I^2$$

and is given by

$$T = \left[\frac{(1-R)^2 \exp(-\alpha_0 L)}{\sqrt{\pi q_0}}\right] \int_{-\infty}^{+\infty} In[1 + q_0^2 \exp(-t^2)]dt,$$

where z' is the propagation distance within the sample, L is the sample length, R is the surface reflectivity, and α_0 is the unsaturated linear absorption coefficient. Here, q_0 is given by $q_0 = \beta(1-R)I_0 L_{eff}$, where I_0 is the on-axis peak intensity and β is the nonlinear absorption coefficient for the 2PA type process. The effective length is $L_{eff} = 1 - \exp(-\alpha_0 L)/\alpha_0$.

The saturation intensity I_s and nonlinear absorption coefficient β could be calculated from the best-fit curves for the experimental data. By substituting $Z_0 = \pi\omega_0^2/\lambda$, the above equation can be rewritten in terms of the wavelength as

$$\beta = 1/L_{eft} I_0 \left(\frac{1 + \frac{Z^2}{\pi^2 \omega_0^4/\lambda^2}}{T_{OA}} - 1 - \frac{Z^2 \lambda^2}{\pi^2 \omega_0^4} \right)$$

and this suggests a relation between nonlinear absorption coefficient and wavelength of excitation as $\beta\alpha A\lambda^2 \pm C$. The equation resembles the equation of a parabola and it clearly emphasizes that nonlinear absorption coefficient varies as square of the wavelength. Considering the positive quadrant of the curve, it can be observed that nonlinear absorption coefficient increases with an increase in the wavelength. However, as a general rule, the 2PA absorption spectrum follows the linear absorption spectrum and is strongly material dependent.

Figures 1 and 2 illustrate the open-aperture Z-scan data of pure rGO, Ag-Fe_2O_3, and Ag-Fe_2O_3 decorated rGO recorded at wavelengths of 700 nm, 800 nm, and 900 nm, respectively. In order to ensure the repeatability, the Z-scan measurements were performed several times and the best data were considered for the analysis and evaluation of NLO coefficients. To understand the experimental data behavior and predict the nature of the nonlinear absorption process, the obtained experimental data (scattered circles) were numerically fitted with the theoretical normalized transmittance (solid line) as proposed in Sheik-Bahae formalism.[28] Figures 2(a) and 2(b) illustrate the OA Z-scans obtained at different excitation wavelengths for rGO and Ag-Fe_2O_3, respectively. In the case of rGO, the presence of the valley-like pattern suggests the presence of reverse saturable absorption (RSA)-like behavior at different excitation wavelengths (700-900 nm). The Z-scan dip at the focus increases with an increase in the wavelength indicating that the strength of RSA behavior is increasing. As the wavelength increases, the probability of 2PA occurrence increases, which significantly varied the strength of nonlinear absorption. For all excitation wavelengths, the experimental data were found to be well fitted for the 2PA equation and can be ascribed due to the n-π* transition of graphene layers (3.2 eV, 388 nm). Here, the excitation energies (1.3-1.7 eV) are below the band structures of the sp^3 matrix (6 eV) and above the sp^2 cluster (0.5 eV), and the electronic states that promote 2PA come to close proximity of sp^2 domains (0.5-6 eV) of graphene layers.[33]

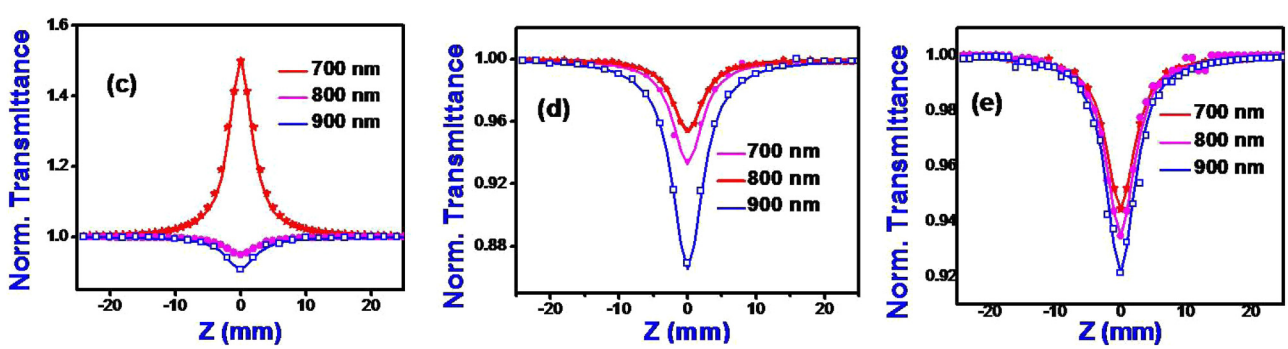

FIG. 2. Open aperture patterns of (c)–(e) Ag-Fe_2O_3–(15, 25, and 40 wt. %)rGO nanocomposite excited with different NIR wavelengths. Symbols are the experimental data points, while the solid lines are theoretical fits.

Thus, observed 2PA of rGO, irrespective of wavelengths, arises from the sp^2 domain of rGO.

In pure Ag-Fe_2O_3 [Fig. 1(b)], at the lowest excitation wavelength of 700 nm, as the sample moved toward beam focus, the normalized transmittance was found to increase (peak pattern), indicating a saturable absorption (SA) behavior, probably arising from plasmon band bleaching. The plasmon band, observed due to collective free-electron oscillations near the nanoparticle surface, is partially bleached in a transient process, heuristically described as saturable absorption and referred to as Fermi smearing. The electrons, thus excited, have a non-equilibrium distribution different from the Fermi–Dirac statistics and lose their energy further by electron–phonon interactions.[34] With 800 nm and 900 nm excitations, the normalized transmittance was found to decrease as the sample moved toward beam focus (valley pattern), thus indicating the existence of reverse saturable absorption. Theoretical fit confirmed that the nonlinear absorption arises due to the 2PA process and involves the electronic states of the ligand-field transition of Fe_2O_3 for 800 nm and the surface plasmon resonance electronic state of Ag nanoparticles for 900 nm excitations. Here, the ligand-field transitions of Fe_2O_3 (2.28 eV) are close to the 2PA state ($2h\nu = 3.10$ eV) of 800 nm and the SPR state of Ag (2.28 eV) is close to the 2PA state ($2h\nu = 2.76$ eV) of 900 nm. Thus, the observed nonlinearity in Ag-Fe_2O_3 composite arises from different band structures such as the plasmon mode of Ag (SA, 700 nm), the ligand field transition of Fe_2O_3 (2PA, 800 nm), and the SPR of Ag (2PA, 900 nm). In the nanocomposites, Ag-Fe_2O_3 nanoparticles are attached to rGO through sp^2 and sp^3 matrix of graphene sheet and oxygen containing functional group, which results in the formation of complex energy state (due to the interaction of Ag-Fe_2O_3 nanoparticles and rGO). The laser pulse causes an interband or intraband electron transition in the decorated Ag-Fe_2O_3–rGO systems, depending on the excitation wavelengths (700-900 nm). In general, the lower energy bandgap in sp^2 matrix is responsible for SA due to the bleaching of valence band (VB) at a lower wavelength (700 nm), while the energy bandgap of sp^3 matrix is larger and laser pulses at 800 nm and 900 nm pumped electrons from VB to conduction band (CB) resulting in a reverse saturable (2PA) absorption. As the wavelength of excitation varies, the condition for 2PA occurrence also varies (700 nm, $2h\nu = 3.56$ eV; 800 nm, $2h\nu = 3.10$ eV; and 900 nm, $2h\nu = 2.76$ eV). Here, the energy state that comes at close vicinity of 2PA state is proposed as the possible transition mechanism. The open-aperture Z-scan measurements on the obtained Ag-Fe_2O_3–rGO nanocomposite are shown in Figs. 2(c)–2(e). For Ag-Fe_2O_3–(15 wt. %) rGO nanocomposite, laser pulses at 700 nm induce SA, while pulses at 800 nm and 900 nm are able to generate 2PA. The pattern resembles the Z-scan curves of pure Ag-Fe_2O_3, and it arises from dominant contribution from Ag-Fe_2O_3 composite due to the higher loading of inorganic component upon the lower content of graphene layers. Plasmon band bleaching in Ag-Fe_2O_3 composite gives rise to saturable absorption (700 nm) and the n-π^* transition of the sp^2 domain of rGO induces the 2PA process (800 and 900 nm) in Ag-Fe_2O_3–(15 wt. %)rGO nanocomposite. However, Ag-Fe_2O_3–(25 and 40 wt. %)rGO nanocomposite exhibits a reverse saturable absorption arising due to the 2PA process. The origin of 2PA involves the electronic states of irregular conjugate carbon bonds based on sp^2 domains of rGO formed during reduction for 700 nm and 800 nm excitations and surface plasmon resonance of Ag metals for 900 nm excitations. It is to be noted here that pure rGO exhibits 2PA at 900 nm and, therefore, in the composite nonlinearity, the contribution of rGO cannot be completely ignored. Since the surface plasmon state of Ag is closer to 2PA excitation state of 900 nm, it is expected that Ag state also possibly

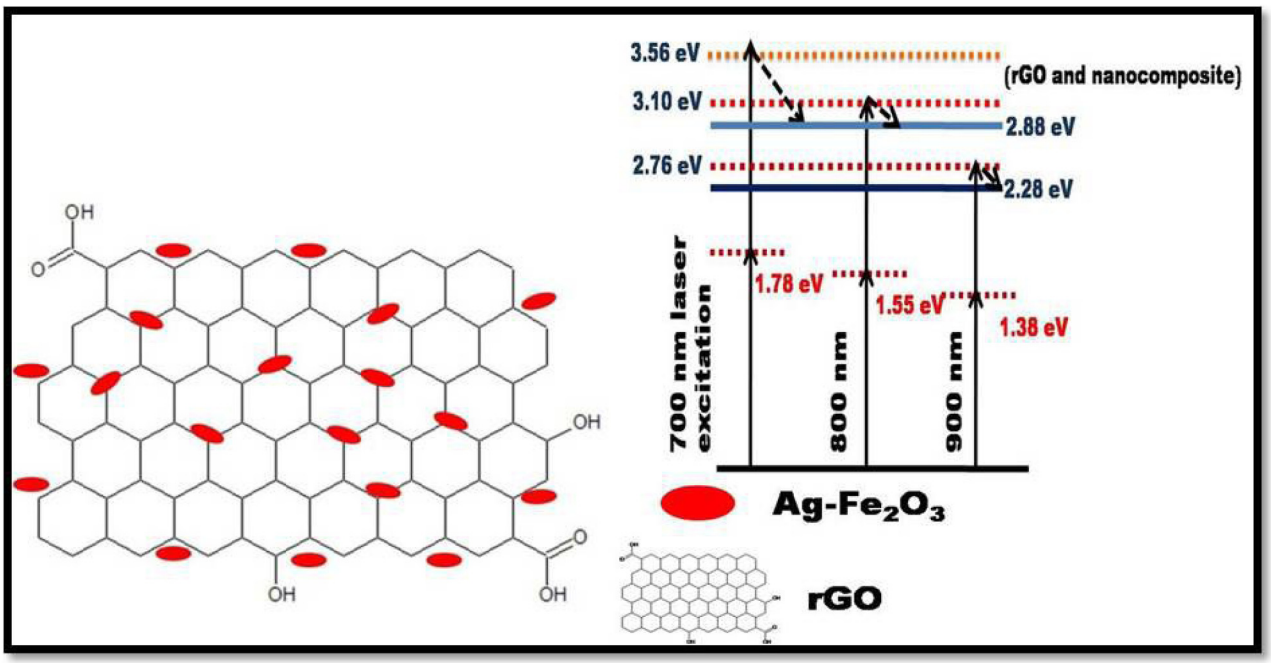

FIG. 3. Energy band diagram of Ag-Fe_2O_3–rGO nanocomposites depicts the electron transfer mechanism with NIR laser excitation.

contributes toward the observed 2PA. Further detailed studies and analysis involving the Z-scan data of pure Ag nanoparticles and pure rGO obtained separately are essential to understand and quantify the exact origin of 2PA in these composites. During the formation of Ag-Fe_2O_3–(15 wt. %) rGO nanocomposite, complex energy levels are formed due to the interaction between the energy levels of Ag-Fe_2O_3 nanospindles and rGO as shown in Fig. 3. Minimal absorption in the wavelength region of excitation suggests that the nonlinear absorption is a genuine 2PA process, rather than a two-step absorption. At 700 nm excitation, a switch in the sign of nonlinear absorption coefficient (positive to negative) takes place as the content of rGO in the nanocomposite increases. Here, the magnitude of nonlinear absorption coefficient at 700 nm varies as Ag-Fe_2O_3–(25 wt. %)rGO > Ag-Fe_2O_3–(40 wt. %) rGO > rGO > Ag-Fe_2O_3–(15 wt. %)rGO > Ag-Fe_2O_3. For other wavelengths (800 nm and 900 nm), nonlinear absorption coefficient varies as Ag-Fe_2O_3–(25 wt. %)rGO > Ag-Fe_2O_3–(40 wt. %)rGO > Ag-Fe_2O_3–(15 wt. %)rGO > Ag-Fe_2O_3 > rGO. In comparison, Ag-Fe_2O_3–(25 wt. %)rGO possesses a higher 2PA coefficient for all chosen wavelengths, thus making them preferable for broadband optical limiting applications. The observed higher NLO coefficients of the investigated materials arise due to the part contribution from thermal nonlinearity (high-repetition rate lasers). As the laser excitation involves high-repetition rate (80 MHz) which is much higher than the thermal diffusion time, cumulative thermal effects also contribute to the Z-scan signal. This thermal dissipated excess energy redistributes among the vibrations in the solute molecules and turns into intramolecular heat. These eventually dissipate into the phonon bath and raise the solution temperature. The change in the refractive index due to diffusive effects has notable applications in optical communication systems operating at a high repetition rate.[29,30]

B. Broadband optical limiting behavior

The optical limiting materials can now be used for the protection of sensitive sensors and devices from laser damage, for anti-glare treated devices, and for optical circuits.[35–38] Literature reveals Wang *et al.*[39] demonstrating broadband OL (1064 nm and 532 nm) behavior in dispersed graphene by the Z-scan technique. Philip *et al.*[40] exposed the non-degenerate 2PA of GO nanosheets with 400-700 nm ultrafast laser pulses. As mentioned earlier, only limited materials are found to exhibit broadband optical limiting against ultrafast lasers. Here, the explored wavelength dependent nonlinear absorption suggests the possibility of utilizing Ag-Fe_2O_3–rGO nanocomposites as broadband optical limiters. To understand the optical limiting, the fluence as a function of position was evaluated from OA pattern with the relation[41] $F(z) = 4\sqrt{\ln 2}\left(\frac{E_{in}}{\pi^{3/2}}\right)\omega(Z)^2$, where F(z) is the input fluence, E_{in} is the laser energy, and ω_o is the laser beam radius at the focus. In Fig. 4 data, the variation of normalized transmittance of pure and decorated Ag-Fe_2O_3–rGO dispersed in ethylene glycol as a function of the laser irradiance through a 1 mm cuvette for 700 nm, 800 nm, and 900 nm is shown. As can be seen, the normalized transmittance with input irradiance under multi-wavelength excitations (700-900 nm) exhibits an excellent broadband limiting performance against the high repetition rate and fs laser pulses. Here, all the samples that exhibit RSA display a rapid decrease in transmittance with a rise in the input fluence at different wavelengths, which is the signature of BOL behavior. The estimated onset OL threshold (input at which the nonlinearity starts) is given in Table I. It is noteworthy that the samples exposed to NIR ultrafast pulse laser with peak intensities of 193-320 MW/cm^2 demonstrated optical limiting action with onset limiting thresholds of 23.11-48.59 μJ/cm^2. And in recent years, femtosecond laser microsurgery that requires energy of ~μJ is getting widely spread. Here, the composite can be used as controllable ultrafast IR laser source emission in microsurgery and sub-surface endoscopic ablation as it limits the output in a microjoule scale.[42] As shown in Table I, rGO and Ag-Fe_2O_3–(25 and 40 wt. %)rGO samples exhibit optical limiting action in all the chosen NIR wavelengths and hence can be recognized as broadband optical limiters, and Ag-Fe_2O_3 and Ag-Fe_2O_3–(15 wt. %)rGO exhibit optical limiting behavior only at 800 nm and 900 nm. A trend in the variation of limiting threshold follows the same variation of nonlinear absorption coefficient. Among the samples, the lowest limiting threshold is observed with Ag-Fe_2O_3–(25 wt. %)rGO for all chosen wavelengths, imposing the potentiality of the material for broadband optical limiting action against ultrashort pulse IR laser. At 900 nm excitation, Ag-Fe_2O_3–(25 wt. %)rGO possessed the lowest limiting threshold of 23.11 μJ/cm^2, which is much lower than the other recently reported oxygenated carbon nanomaterials and functionalized-hydrogen exfoliated graphene (f-HEG) graphene composite.[32]

From the numerical fit, the estimated $\beta_{SA/2PA}$ of the samples is tabulated in Table I. It can be clearly evidenced that with an increase in the wavelength of excitation, the nonlinear absorption coefficient also increases. Strong nonlinear absorption coefficient at 900 nm is not only due to the involved longer wavelength exposure but also because of the contribution arising from the surface plasma resonance of Ag metal nanoparticles. Here, Ag-Fe_2O_3–(25 wt. %)rGO possess a higher 2PA coefficient compared to Ag-Fe_2O_3–(15 and 40 wt. %)rGO. The larger extent of conjugation in graphene surface due to the removal of oxygen containing functional groups, large metals' (Ag-Fe_2O_3) nonlinear response, and the local field effect contribute to enhanced NLO response in Ag-Fe_2O_3 decorated rGO. Also, the enhancement in nonlinear absorption mainly arises because of the defect induced states originating due to functionalization of rGO, which facilitate interband transition [as discussed in Raman analysis, I_D/I_G ratio is 0.75, 0.88, and 0.65 for Ag-Fe_2O_3–(15, 25, and 40 wt. %)rGO]. Also, Ag-Fe_2O_3 being a stronger 2PA system than rGO, the involvement of Ag-Fe_2O_3 (SPR state of Ag) in achieving 2PA at 900 nm resulted in the maximum 2PA coefficient not only with Ag-Fe_2O_3–(25 wt. %)rGO but also with other composites. Hence, it can be concluded that the loading of Ag-Fe_2O_3 on rGO has a direct influence on the overall 2PA performance.

The 2PA coefficient (β_{2PA}) of well-understood OL materials such as pure reduced graphene oxide (10^{-13})[43,44] and

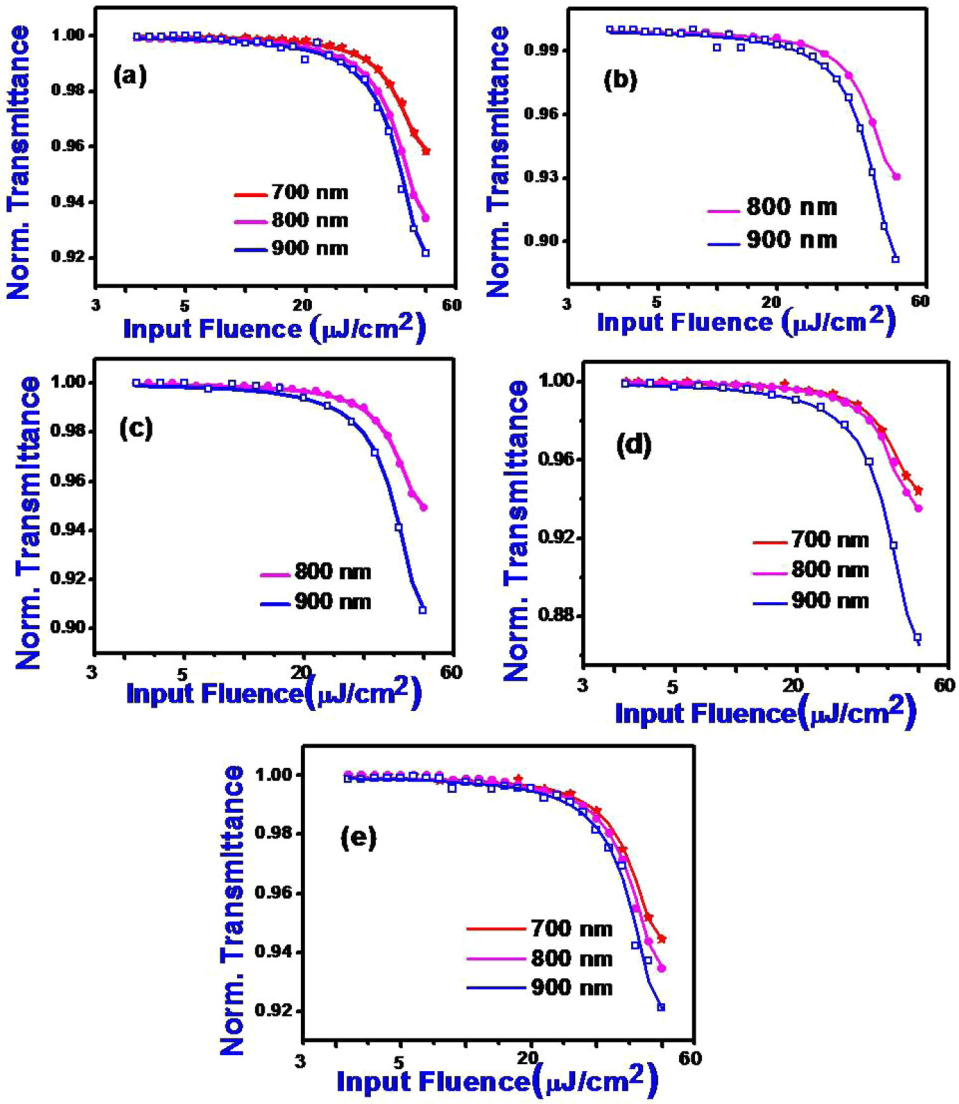

FIG. 4. Optical limiting behavior of (a) rGO, (b) Ag-Fe_2O_3, and (c)–(e) Ag-Fe_2O_3–(15, 25, and 40 wt. %)rGO nanocomposite excited with different NIR wavelengths. Symbols are the experimental data points, while the solid lines are theoretical fits.

functionalized hydrogen exfoliated graphene (10^{-15} m/W)[32] is comparatively few orders lower than decorated Ag-Fe_2O_3–rGO nanocomposite. Among the investigated samples, a maximum nonlinear absorption coefficient of 6.0×10^{-10} m/W was observed with Ag-Fe_2O_3–(25 wt. %)rGO at an excitation wavelength of 900 nm. The reason for enhanced optical nonlinearity in Ag-Fe_2O_3–(25 wt. %)rGO can be explained as follows: high I_D/I_G ratio (0.88) for the graphene content of (25 wt. %)rGO functionalization suggests more defects in the decorated systems. As newly formed sp^2 carbon domains are smaller in size, the sp^2 domain crystallite size (La = 7.9 nm) is lower for Ag-Fe_2O_3–(25 wt. %)rGO compared to that of rGO and other Ag-Fe_2O_3–(15 and 40 wt. %)rGO composites. So, an increase in β_{2PA} of Ag-Fe_2O_3–(25 wt. %)rGO nanocomposite is dominantly due to the increase in the defect induced states upon Ag-Fe_2O_3 functionalization. Also, the TEM results of Ag-Fe_2O_3–rGO nanocomposite reveal that the crumpled silk waves of rGO sheets are loaded heavily with Ag-Fe_2O_3 compared to other composites. This provides the dominant contribution from Ag-Fe_2O_3 in 25 wt. % rGO

TABLE I. Estimated nonlinear absorption coefficient and onset optical limiting threshold of the compounds used in this study.

	Excitation wavelength of Ti:Sapphire laser (150 fs, 80 MHz)					
	Nonlinear absorption coefficient ($\beta \times 10^{-10}$ m/W)			Onset optical limiting threshold (μJ/cm^2)		
Samples	700 nm	800 nm	900 nm	700 nm	800 nm	900 nm
rGO	0.5 ± 0.02 (RSA)	1.1 ± 0.05 (RSA)	1.6 ± 0.08 (RSA)	48.59	47.55	46.40
Ag-Fe_2O_3	−14.12 ± 0.70 (SA)	1.9 ± 0.09 (RSA)	2.5 ± 0.12 (RSA)	…	39.11	37.55
Ag-Fe_2O_3–(15 wt. %)rGO	−13.0 ± 0.65 (SA)	2.8 ± 0.14 (RSA)	3.6 ± 0.18 (RSA)	…	36.40	34.26
Ag-Fe_2O_3–(25 wt. %)rGO	2.8 ± 0.14 (RSA)	3.8 ± 0.19 (RSA)	6.0 ± 0.3 (RSA)	30.96	28.31	23.11
Ag-Fe_2O_3–(40 wt. %)rGO	2.2 ± 0.11 (RSA)	3.1 ± 0.15 (RSA)	4.1 ± 0.20 (RSA)	31.93	29.44	24.78

composite, thus resulting in a higher 2PA coefficient. Moreover, a maximum 2PA coefficient is also because of the one-dimensional morphologies (nanospindle as explored in TEM) of Ag-Fe_2O_3 due to the shortened carrier transportation path. This clearly suggests the superiority of densely decorated Ag-Fe_2O_3 upon (25 wt. %)rGO for broadband optical limiting applications as the 2PA coefficient is found to be maximum for all excitation wavelengths. Although the experiments were performed on an automated Z-scan experimental setup, errors in the estimation of focal spot size, peak intensities, and fitting procedures are unavoidable. Hence, based on repeated measurements, the maximum error was estimated to be ~5%.

III. EXPERIMENTAL DETAILS

A. Preparation of graphene oxide (GO), solar exfoliated graphene (rGO), and Ag-Fe_2O_3–rGO nanocomposite

Initially, graphite oxide (GO) was obtained from graphite by the modified Hummer's method,[45] in which graphite was oxidized by treatment with $KMnO_4$ and $NaNO_3$ in concentrated H_2SO_4. The reduction of graphene oxide using reducing agents involves the generation of the toxic gases NO_2, N_2O_4, and/or ClO_2.[46] To overcome this environment hazard, in recent years, the reduction of graphene oxide is achieved through exfoliation with the aid of electromagnetic natural radiations. In the employed solar exfoliation, solar radiation focused as high intensity is directed toward graphene oxide imparting a photoacoustic effect, and the induced localized thermal excitation (~200 °C in 2 s) causes the exfoliation of GO into rGO through deflagration (expelling the oxygen containing functional groups in the form of CO_2 and H_2O). Here, the rapid color change (light brown to dark black), volume expansion, and dense to fluffy change indicate the de-oxygenation of GO.[47] Employing one-step hydrothermal reaction of $Ag(NO_3)_2 \cdot 6H_2O$ and $Fe(NO_3)_3 \cdot 9H_2O$ taken with a molar ratio of 1:2 and in the presence of various rGO contents (40, 25, and 15 wt. %), the Ag-Fe_2O_3–rGO nanocomposite was prepared using a 150 ml Teflon-lined stainless-steel autoclave heated at 180 °C for 12 h. The obtained precipitate was filtered, washed with distilled water several times, and dried in an oven at 60 °C for 24 h. Pure Ag-Fe_2O_3 nanoparticles were prepared by a similar treatment without using rGO.

IV. STRUCTURAL CONFIRMATION

A. Chemical and crystal structure

XPS analysis was performed to investigate the chemical state of rGO and Ag-Fe_2O_3–rGO nanocomposites. In Fig. 5(a), the survey spectra clearly indicate the existence of C, O in rGO, and C, O, Ag, and Fe in the Ag-Fe_2O_3–rGO nanocomposite. In the XPS survey spectrum of rGO, only two main peaks were observed at 285.3 eV and 529.7 eV, which correspond to the carbon (C) and oxygen (O) environment of rGO. The C 1s XPS core level spectrum of reduced graphene oxide can be de-convoluted into three parts with binding energies at 285.0 eV (C=C/C—C in aromatic ring), 286.5 eV (C—O—C), and 288.8 eV (C=O). These results indicated that there are few functional groups left out on the surface of the rGO nanosheets.

In the XPS spectra of the Ag-Fe_2O_3 nanocomposite [Fig. 5(b)], apart from the two main peaks around 285.3 eV and 528.3 eV, which correspond to the C 1s and O 1s species of rGO, three additional peaks of Ag-Fe_2O_3, namely, Ag $3d_{5/2}$, Fe 3p, and Fe $2p_{3/2}$, were observed. The intensity of the band at 288.8 eV (C=O) comparatively decreased, which indicates the further reduction of rGO nanosheets due to functionalization. The appearance of Ag 3d and Fe 2p signals along with rGO indicates that Ag and Fe_2O_3 nanoparticles were successfully assembled onto the rGO surface. The C 1s, Ag 3d, and Fe 2p core level spectra of nanocomposite are shown in Figs. 5(c)–5(e). The de-convoluted spectrum of nanocomposite clearly shows the presence of main peaks at 285.07 (C=C), 285.31 (C—O), 288.88 eV (C=O); 386.29, 374.26 eV (Ag 3d); and 711.11, 724.00 eV (Fe 2p). Here, the peak values corresponding to C 1s state are shifted to higher energy, which is due to the effect of further reduction of rGO upon functionalization.

XRD measurements (Fig. 6) were carried out to make the preliminary confirmation of nanocomposite formation and also to investigate the crystal phases of the typical product. XRD of the samples obtained from the Hummer's method shows a peak at $2\theta = 10.6°$ which corresponds to the (001) plane of GO.[48] The absence of any peak at 2θ=26° reveals that the oxidization process is complete and the formed GO is devoid of any graphite. The XRD of solar exfoliated graphene oxide gives the first confirmation of the complete reduction of GO, through the disappearance of a peak at $2\theta = 10.6°$, and the formation of new weak and broad peak at $2\theta = 24°$ representing the (002) plane of rGO. The broadening of graphene peak in the XRD pattern of exfoliated sample can be attributed to the small size of the layers or a relatively short domain order of the stacked sheets. This is because, due to the fast heating of graphene oxide, the rate of decomposition of oxygen containing functional groups is higher than the diffusion rate of the evolved gases returning back to graphene, thus yielding a pressure that surmounts the Van der Waals force holding the graphene sheets. In the XRD pattern of products from hydrothermal reaction, the presence of rGO peak [$2\theta = 24°$, (002)] is accompanied by many well-distinct crystalline peaks arising from the incorporated elements. The recorded XRD of Ag-Fe_2O_3–(15, 25, and 40 wt. %)rGO nanocomposites shows diffraction peaks at $2\theta = 33.3$, 35.7, 49.5, 54.1, 62.7, 77.5, and 38.3, 44.5, 64.8 corresponding to (104), (311), (024), (116), (214), (036), and (111), (200), (220) planes of Ag [Joint Committee for Powder Diffraction Standards (JCPDS): 89-3722] and Fe_2O_3 (JCPDS: 89-8104), respectively. A small shift in peak position was due to the variation in the loading of Ag-Fe_2O_3 on different contents of rGO. The diminishing nature of diffraction peaks of Fe_2O_3 is most likely due to the heavy atom effect from silver in the Ag-Fe_3O_3 nanoparticles. Thus, a chemical state and XRD study clearly confirm the formation of desired nanocomposites, i.e., Ag-Fe_2O_3–rGO.

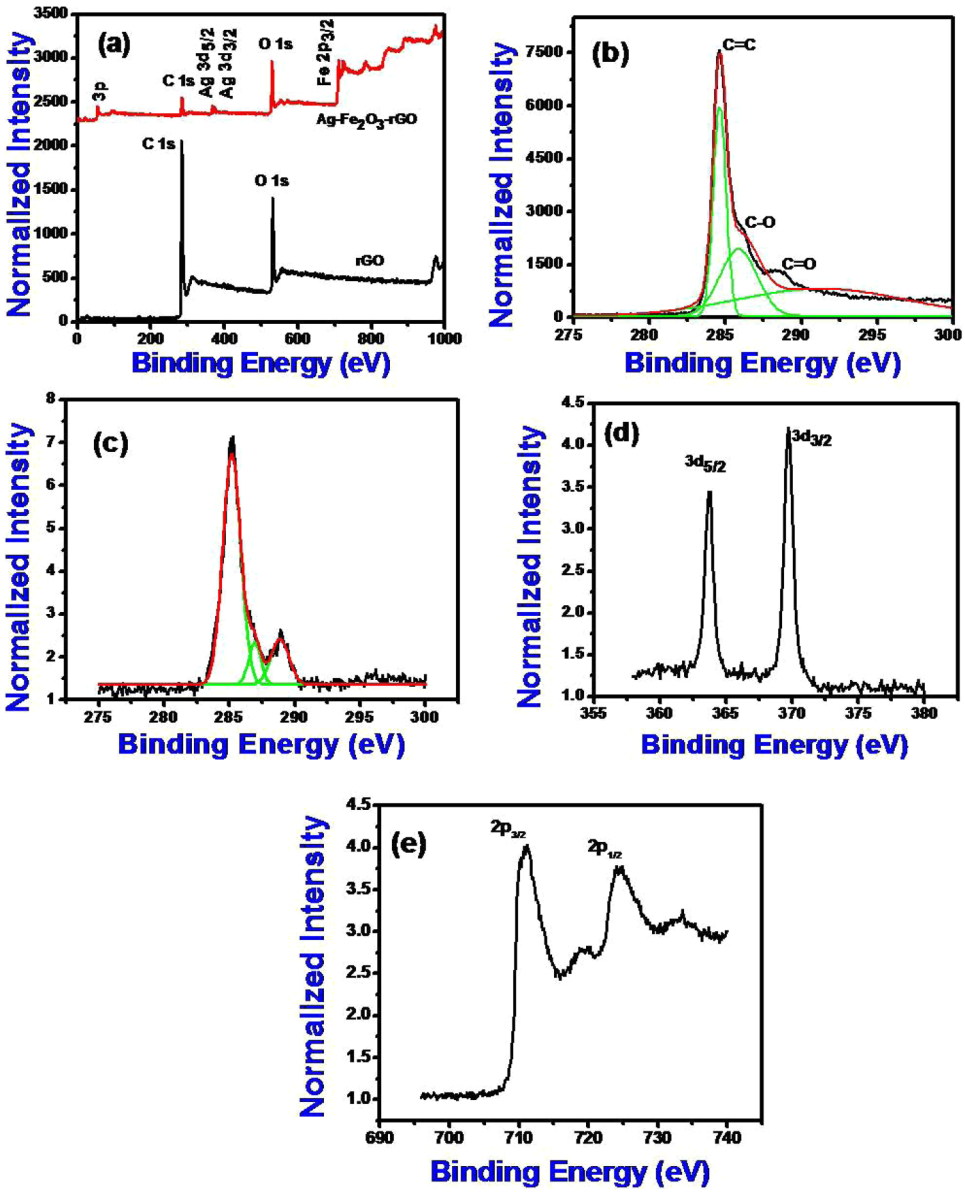

FIG. 5. XPS spectra of (a) rGO and Ag-Fe_2O_3–(15 wt. %)rGO nanocomposites, (b) C 1s XPS spectra of rGO, (c) Ag-Fe_2O_3–(15 wt. %)rGO nanocomposites, (d) Ag 3d, (e) Fe 2p core level spectrum of Ag-Fe_2O_3–(15 wt. %)rGO nanocomposites. The peaks of (b) and (c) were fitted with Gaussian curves, and the green lines represent the components of Gaussian fit made on C 1s XPS spectrum.

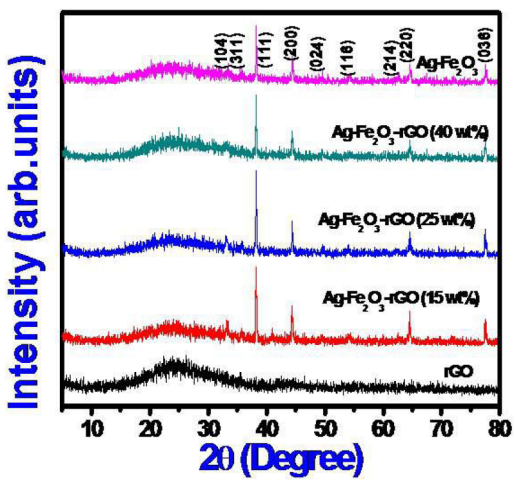

FIG. 6. XRD spectrum of pure rGO, Ag-Fe_2O_3, and Ag-Fe_2O_3–(15 wt. %, 25 wt. %, and 40 wt. %)rGO nanocomposites.

B. Morphology and defect states

SEM was used to characterize the morphologies of rGO, Ag-Fe_2O_3, and Ag-Fe_2O_3–rGO nanocomposites. The recorded SEM of rGO (as shown in Fig. 7) is manifesting that most of the GOs were efficiently exfoliated to form well separated, ultrathin, and transparent graphene sheets. The Ag-Fe_2O_3 form themselves as nanospindles and in Ag-Fe_2O_3–rGO nanocomposites, spindles were randomly dispersed on the rGO nanosheet surfaces appearing as bright spots. In principle, a crystal growth process consists of nucleation and growth, which are affected by the intrinsic crystal structure and the external condition. The nucleation of the Ag-Fe_2O_3 occurs through the interaction of Ag^+ and Fe^{3+} ions with the negatively charged —COOH or —C_2H_4 or —OH groups on graphene sheets, which serves as anchoring sites for the growth of Ag-Fe_2O_3 nanoparticles. On the graphene sheets, initially Ag-Fe_2O_3 form themselves

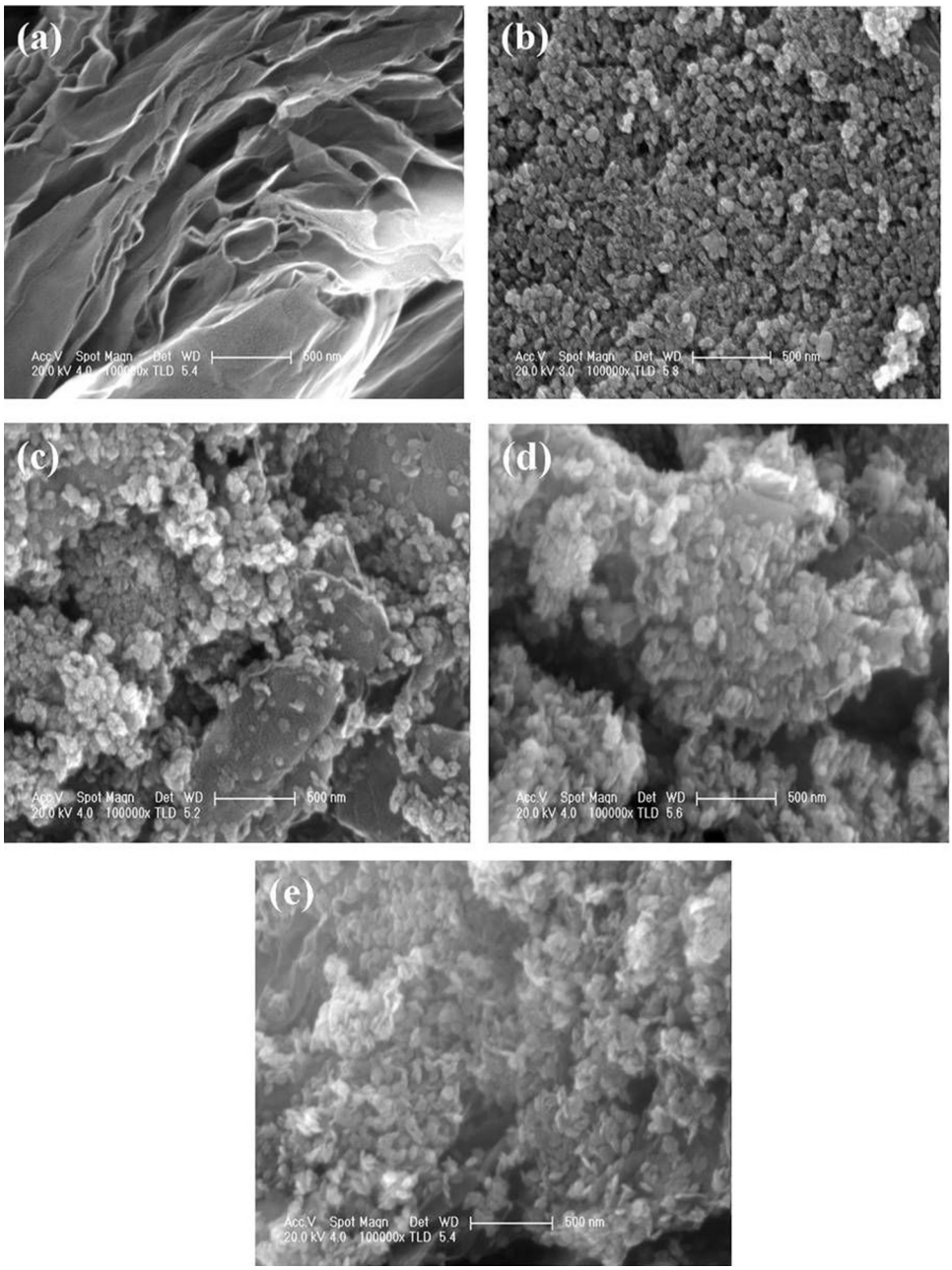

FIG. 7. SEM images of (a) rGO, (b) Ag-Fe_2O_3, and (c)–(e) Ag-Fe_2O_3–(15, 25, and 40 wt. %)rGO nanocomposites.

as stable nanospheres and then aggregate due to cohesion to form as nanospindles. The carboxylic anions especially have a strong chelating effect on transition metal ions and therefore Ag-Fe_2O_3 spindle was distributed throughout the rGO sheet due to the coordination between hydroxyls and Ag-Fe_2O_3. The combination of Ag-Fe_2O_3 spindle and graphene made the surface of the graphene rough, which created favorable conditions for loading more Ag-Fe_2O_3 NPs. A variation in the loading of Ag-Fe_2O_3 with content of rGO is clearly witnessed in the recorded SEM images.

Figure 8 illustrates the TEM images of rGO and Ag-Fe_2O_3–rGO nanocomposite. It can be clearly seen in Fig. 8(a) that rGO nanosheets display wrinkled ultrathin sheets with silk-like morphology suggesting the full exfoliation of rGO sheets. The spindle-like structure with an average size of 55×30 nm was observed for pure Ag-Fe_2O_3. For the Ag-Fe_2O_3–(15 wt. %, 25 wt. %, and 40 wt. %)rGO nanocomposite, nanospindles of Ag-Fe_2O_3 are uniformly distributed or wrapped like a sandwich, which indicate a firm interaction between the two materials. The relative size of Ag-Fe_2O_3 on (15-40 wt. %)rGO was about (69×21 nm), (74×26 nm), and (74×32 nm), respectively. The corresponding selected area electron diffraction (SAED) pattern [inset of Figs. 7(b)–7(e)] of the pure Ag-Fe_2O_3 and Ag-Fe_2O_3–rGO nanocomposites shows diffraction rings with a bright spot, which signifies the polycrystalline nature of the materials.

The Raman spectroscopy is a powerful technique for studying disorder and defects in the crystal structure of pure and decorated systems. The Raman spectra of graphene-based materials were performed on a Renishaw in Via Raman microscopy with 532 nm laser as the excitation

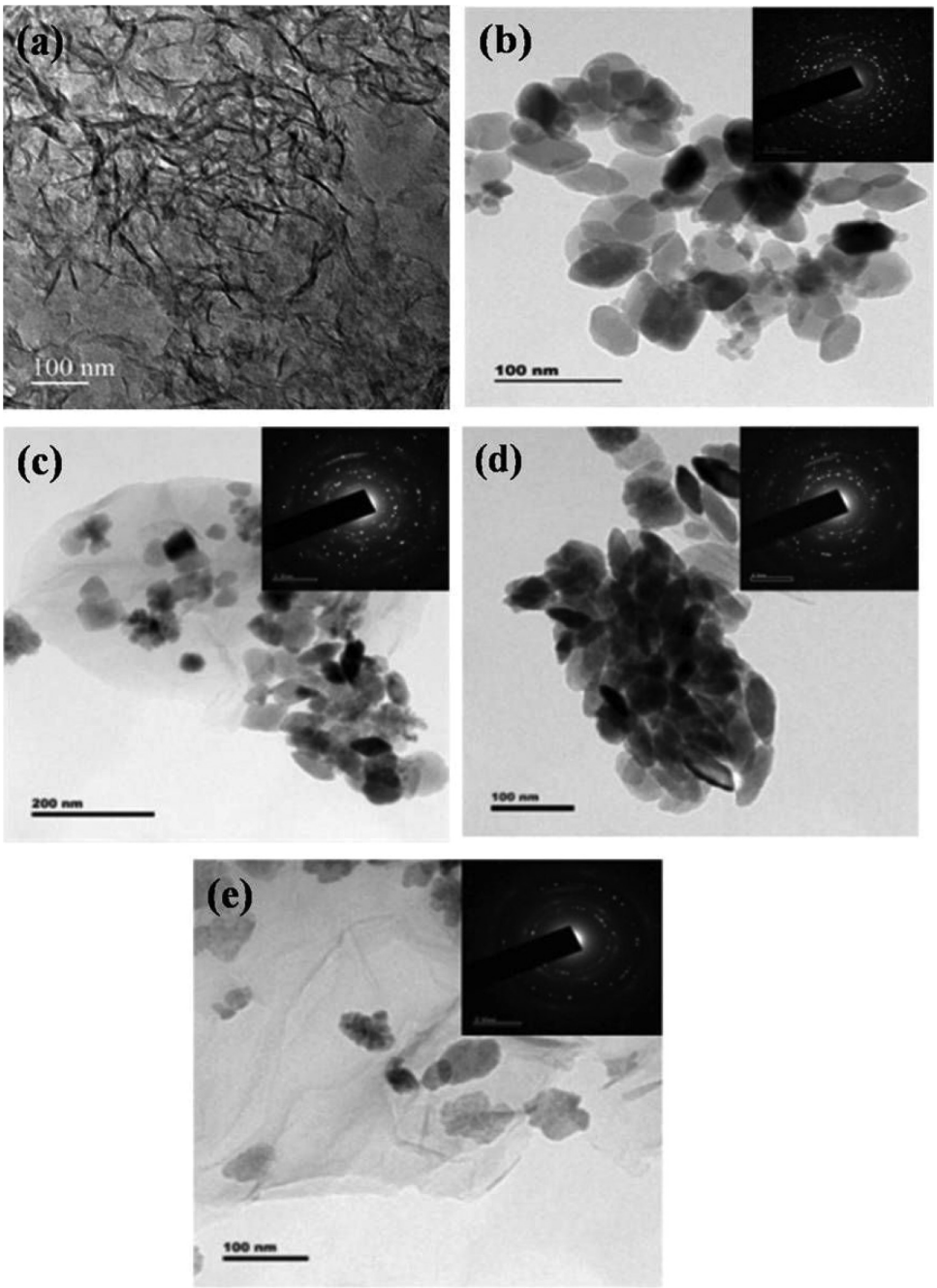

FIG. 8. TEM images of (a) rGO (wrinkled silk), (b) Ag-Fe_2O_3, and (c)–(e) Ag-Fe_2O_3–(15, 25, and 40 wt. %)rGO nanocomposites (spindle of Ag-Fe_2O_3 upon thin graphene layers) and the corresponding SAED pattern (inset).

source. Disorder is determined by the intensity ratio between the disorder induced D band and the Raman allowed G band (I_D/I_G). The Raman spectra of the reduced graphene oxide, Ag-Fe_2O_3, and Ag-Fe_2O_3–rGO nanocomposite areas are shown in Fig. 9. The G band is observed at 1607 cm^{-1} and 1598 cm^{-1} and the D band at 1358 cm^{-1} and 1342 cm^{-1} originating from C—C stretching of sp^2 carbon forms for rGO and Ag-Fe_2O_3–rGO, respectively. The I_D/I_G of rGO and Ag-Fe_2O_3–(15, 25, 40 wt. %)rGO nanocomposites was determined to be 0.78, 0.75, 0.88, and 0.65, respectively. The increase in the ratio of I_D/I_G of Ag-Fe_2O_3–rGO was recognized due to the reduction of GO to rGO in the process of synthesis of Ag-Fe_2O_3–rGO. Furthermore, using the I_D/I_G ratio, the size of the perfect graphene domain (L_a) was estimated[49] to be ~8.9 nm for rGO, which upon functionalization increases to 9.3 nm, 7.9 nm, and 10.9 nm for Ag-Fe_2O_3–(15 wt. %, 25 wt. %, and 40 wt. %)rGO, respectively. The six Raman modes at 221, 290, 407, 480, and 661 cm^{-1} represent the Raman modes ($A_{1g} + E_g$) of Fe_2O_3. Furthermore, the strong peaks observed at 973, 842, 1072, 1320, and 1588 cm^{-1} arise due to Ag, which exhibits its presence in the Ag-Fe_2O_3 hybrid structure. The hybrid formation might be due to the synergetic effect of defective crystalline structures of Ag with Fe_2O_3 nanospindles. In fact, the de-oxygenation of the rGO sheets during the hydrothermal reaction could have resulted in the reduction of I_D/I_G ratio, thereby confirming the formation of chemical bond between the Ag-Fe_2O_3 and rGO sheets.

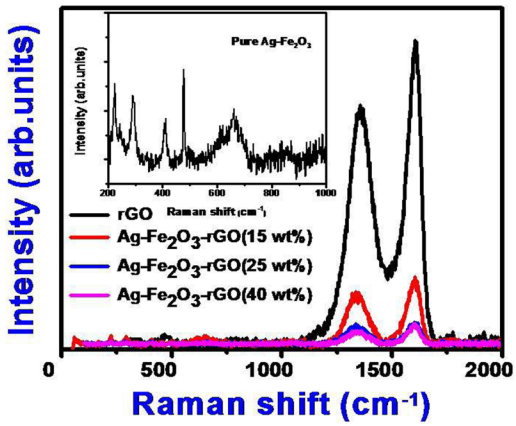

FIG. 9. Raman spectra of Ag-Fe_2O_3–(15 wt. %, 25 wt. %, and 40 wt. %)rGO nanocomposites and pure Ag-Fe_2O_3 (inset).

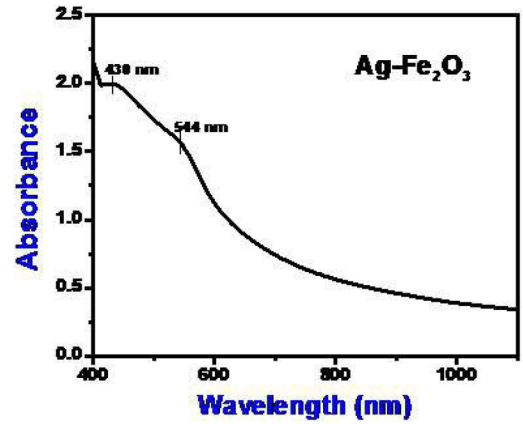

FIG. 11. UV-visible absorption spectra of pure Ag-Fe_2O_3.

V. GROUND STATE ABSORPTION

A. UV-visible absorption studies

The UV-visible absorption (Fig. 10) spectra of GO show an absorption peak at 230 nm and a shoulder peak at 260 nm corresponding to the π-π* and n-π transitions, while after solar exfoliation, reduction to rGO red shifts the absorption maximum to 270 nm and 388 nm arising due to the restoration of sp^2 carbon domains. In the absorption (Fig. 11) pattern of Ag-Fe_2O_3, the peaks at 430 nm, representing the ligand-field transitions of ferric oxide (pair-excitation), and 544 nm are due to the contribution of surface plasmon resonance peak of Ag nanoparticles. The dominance of SPR state of Ag has possibly suppressed the absorption peaks arising from ferric oxide in the composite. The optical properties of Ag-Fe_2O_3 are evidently individual, thus demonstrating that these materials are nanocomposite structures. For the nanocomposite, the π-π* transition state of rGO, the ligand-field transitions of Fe_2O_3, and the SPR peak of Ag nanoparticle arise at 267 nm, 431 nm, and 544 nm (40 wt. %); 260 nm, 434 nm, and 541 nm (25 wt. %); and 262 nm, 433 nm, and 545 nm (15 wt. %), respectively. Thus, the electronic band structure gets strongly altered through composite formation, and the availability of different energy states (due to Ag, Fe_2O_3, and rGO) provides the opportunity for the system to be used as broadband optical limiters.

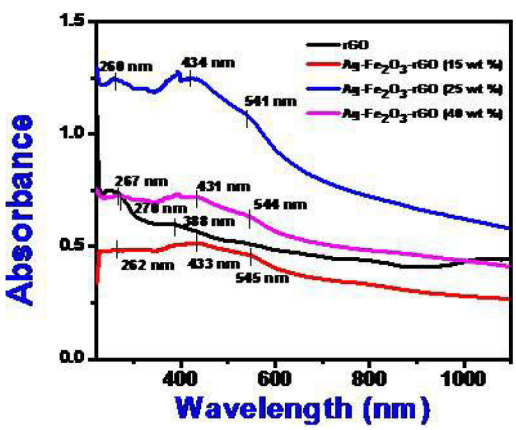

FIG. 10. UV-visible absorption spectra of pure rGO and Ag-Fe_2O_3–(15 wt. %, 25 wt. %, and 40 wt. %)rGO nanocomposites.

VI. CONCLUSIONS

The synthesis, structure, and the NLO properties of pure rGO, Ag-Fe_2O_3, and Ag-Fe_2O_3–rGO nanocomposites were reported. The results of XPS, XRD, SEM, TEM, Raman, and UV-vis absorption spectra confirm the successful fabrication of hybrid materials based on covalent functionalization and electrostatic adsorption between rGO and Ag-Fe_2O_3. Wavelength dependent nonlinear absorption and ultrafast optical limiting of reduced graphene oxide, Ag-Fe_2O_3, and Ag-Fe_2O_3–rGO nanocomposite in the infrared region (700-900 nm) by a single ultrafast Z-scan measurement were studied. Both Ag-Fe_2O_3 and Ag-Fe_2O_3–(15 wt. %)rGO exhibited a switching behavior from SA to RSA as the wavelength of excitation increased from 700 nm to 900 nm. All other samples exhibit RSA behavior ascribed due to the 2PA process. Furthermore, the magnitude of 2PA coefficient was found to increase with the wavelength of excitation. Here, the SA behavior was ascribed to the ground state plasmon band bleaching and RSA (2PA) due to the involvement of the interband transition in the electronic states of the sp^2 domain of rGO (700 nm and 800 nm) and the SPR of Ag metal (900 nm). The competition between different processes is responsible for the observed switching behavior. Therefore, from a device's point of view, Ag-Fe_2O_3–rGO nanocomposites possess a unique advantage: depending on the excitation wavelengths, they can potentially be used for laser safety applications (OL behavior) or pulse shaping, shortening, and optical switching (SA behavior).

ACKNOWLEDGMENTS

T. C. Sabari Girisun acknowledges the financial support from CSIR, India [03(1375)/16/EMR-II] and Raman facility from DST-FIST, India [SR/FST/PSI-204/2015(C)]. S. Venugopal Rao acknowledges the financial support from DRDO, India.

[1]U. Keller, Nature **424**, 831 (2003).
[2]A. H. Zewail, Science **242**, 1645 (1988).
[3]D. Stuart Jackson, Nat. Photon. **6**, 423 (2012).

[4]K. Sugioka and Y. Cheng, Appl. Phys. Rev. **1**, 041303 (2014).
[5]C. M. B. Ho, A. Mishra, K. Hu, J. An, Y. J. Kim, and Y. J. Yoon, ACS Biomater. Sci. Eng. **3**, 2198 (2017).
[6]L. Yanyan, X. Meng, H. Wang, Z. Tang, C. Zuo, M. He, and W. Bu, ACS Appl. Mater. Interfaces **10**, 1492 (2018).
[7]C. Xu and F. W. Wise, Nat. Photon. **7**, 875 (2013).
[8]B. Quentin, B. Pierre-Antoine, K. Kamada, P. Feneyrou, E. Malmström, O. Maury, and C. Andraud, Opt. Mater. Def. Syst. Technol. **6**, 7487 (2009).
[9]S. Kishore, P. Sreekanth, T. J. Park, and R. Philip, J. Phys. Chem. C **119**, 16314 (2015).
[10]B. Anand, S. A. Ntim, V. Sai Muthukumar, S. S. S. Sai, R. Philip, and S. Mitra, Carbon **49**, 4767 (2011).
[11]L. Yongsheng, J. Zhou, X. Zhang, Z. Liu, X. Wan, J. Tian, T. Wang, and Y. Chen, Carbon **47**, 3113 (2009).
[12]Z. Sun, N. Dong, K. Wang, D. König, T. C. Nagaiah, M. D. Sánchez, A. Ludwig, X. Cheng, W. Schuhmann, J. Wang, and M. Muhler, Carbon **62**, 182 (2013).
[13]Y. J. Kim, J. Lee, K. Lee, S. Han, Y. S. Jang, H. Jang, and S. W. Kim, "Optical sensors," in *Proceedings Advanced Photonics, Rio Grande, PR, 14–17 July 2013* (OSA, 2013), SW4B-1.
[14]P. A. Bouit, G. Wetzel, G. Berginc, B. Loiseaux, L. Toupet, P. Feneyrou, Y. Bretonniere, K. Kamada, O. Maury, and C. Andraud, Chem. Mater. **19**, 5325 (2007).
[15]B. Sudhakara Reddy, P. B. Bisht, C. K. R. Namboodiri, P. Nayak, S. Ramaprabhu, J. T. Kelly, C. Fallon, and T. J. Costello, J. Appl. Phys. **116**, 073101 (2014).
[16]W. Yusong, L. Polavarapu, and M. Luis Liz-Marzán, ACS Appl. Mater. Interfaces **6**, 21798 (2014).
[17]F. Miao, H. Zhan, and Y. Chen, Appl. Phys. Lett. **96**, 033107 (2010).
[18]N. Liaros, P. Aloukos, A. Kolokithas-Ntoukas, A. Bakandritsos, T. Szabo, R. Zboril, and S. Couris, J. Phys. Chem. C **117**, 6842 (2013).
[19]Z. Chan, W. Chen, Y. Huang, X. Xiao, and X. Ye, RSC Adv. **4**, 39697 (2014).
[20]Y. Chen, Y. Zhang, F. Pan, J. Liu, K. Wang, C. Zhang, S. Cheng, L. Lu, W. Zhang, Z. Zhang, and X. Zhi, ACS Nano **10**, 8169 (2016).
[21]K. P. Loh, Q. Bao, G. Eda, and M. Chhowalla, Nat. Chem. **2**, 1015 (2010).
[22]Q. Guo, Y. Yao, Z. C. Luo, Z. Qin, G. Xie, M. Li, J. Kang, S. Zhang, G. Bi, X. Liu, and J. Qiu, ACS Nano **10**, 9463 (2016).
[23]G. Gil, A. A. P. Paula Marques, M. C. Granadeiro, I. S. H. Nogueira, M. K. Singh, and J. Gracio, Chem. Mater. **21**, 4796 (2009).
[24]G. Xing, J. Jiang, J. Y. Ying, and W. Ji, Opt. Express **18**, 6183 (2010).
[25]M. Yue, J. Si, L. Yan, Y. Yu, and X. Hou, Opt. Mater. Express **8**, 698 (2018).
[26]B. S. Kalanoor, P. B. Bisht, S. A. Ali, T. T. Baby, S. Ramaprabhu, J. Opt. Soc. Am. B **29**, 669 (2012).
[27]R. L. Sutherland, *Handbook of Nonlinear Optics* (Mercel Dekker Inc., 1996).
[28]M. Sheik-Bahae, A. A. Said, T.-H. Wei, D. J. Hagan, and E. W. Van Stryland, IEEE J. Quantum Electron. **4**, 760 (1990).
[29]M. Falconieri, J. Opt. A: Pure Appl. Opt. **1**, 662–667 (1999).
[30]N. Liaros and J. T. Fourkas, Laser Photon. Rev. **11**, 1700106 (2017).
[31]P. Chantharasupawong, R. Philip, T. Narayanan, P. M. Sudeep, A. Mathkar, M. P. Ajayan, and J. Thomas, J. Phys. Chem. C **116**, 25955 (2012).
[32]B. Anand, A. Kaniyoor, S. S. S. Sai, R. Philip, and S. Ramaprabhu, J. Mater. Chem. C **1**, 2773 (2013).
[33]S. Hongfei, C. Wang, Z. Sun, Y. Zhou, K. Jin, S. A. T. Redfern, and G. Yang, Opt. Express **22**, 19375 (2014).
[34]V. Liberman, M. Sworin, R. P. Kingsborough, G. P. Geurtsen, and M. Rothschild, J. Appl. Phys. **113**, 053107 (2013).
[35]T. Xia, D. J. Hagan, A. Dogariu, A. A. Said, and E. W. Van Stryland, Appl. Opt. **36**, 4110 (1997).
[36]W. Jun, Y. Chen, R. Li, H. Dong, Y. Ju, J. He, and J. Fan, J. Inorg. Organmet. Polym. Mater. **21**, 736 (2011).
[37]G. K. Lim, Z. L. Chen, J. Clark, G. S. Roland Goh, N. G. Wee Hao, H. W. Tan, H. Richard, K. H. Peter Ho, and L. L. Chua, Nat. Photon. **5**, 554 (2011).
[38]C. P. Singh and K. S. Bindra, Opt. Quantum Electron. **47**, 313 (2015).
[39]A. J. Wang, W. Yu, Y. Fang, Y. L. Song, D. Jia, L. L. Long, M. P. Cifuentes, M. G. Humphrey, and C. Zhang, Carbon **89**, 130 (2015).
[40]P. Sreekanth, P. Sankar, T. P. Rose, and R. Philip, Appl. Phys. Lett. **107**, 051104 (2015).
[41]M. Saravanan, T. C. Sabari Girisun, G. Vinitha, and S. Venugopal Rao, RSC Adv. **6**, 91083 (2016).
[42]S. Kaushik, I. Gabay, O. Ferhanoğlu, A. Shadfan, M. Pawlowski, Y. Wang, T. Tkaczyk, and A. Ben Yakar, Biomed. Opt. Express **7**, 4639 (2016).
[43]S. R. Bongu, P. B. Bisht, R. C. Namboodri, P. Nayak, S. Ramaprabhu, T. J. Kelly, C. Fallon, and J. T. Costello, J. Appl. Phys. **116**, 073101 (2014).
[44]R. P. Ummer, P. Sreekanth, B. Raneesh, R. Philip, D. Rouxel, S. Thomas, and N. Kalarikkal, RSC. Adv. **5**, 67157 (2015).
[45]M. Alireza and O. Akhavan, Carbon **69**, 230 (2014).
[46]M. C. Daniela, V. D. Kosynkin, M. J. Berlin, A. Sinitskii, Z. Sun, A. Slesarev, L. B. Alemany, W. Lu, M. James, and M. Tour, ACS Nano **4**, 4806 (2010).
[47]E. Varrla, S. Sasikaladevi, J. Aravind, and S. Ramaprabhu, J. Mater. Chem. **21**, 6800 (2011).
[48]M. Saravanan, T. C. Sabari Girisun, and G. Vinitha, J. Mol. Liq. **256**, 519 (2018).
[49]M. Saravanan and T. C. Sabari Girisun, Appl. Surf. Sci. **392**, 904 (2017).